

A compact actively damped vibration isolation platform for optical experiments in ultra-high vacuum

Álvaro Fernández Galiana,^{1,2,a)} Lee McCuller,¹ Jeff Kissel,³ Lisa Barsotti,¹ John Miller,¹ Maggie Tse,^{1,4} Matthew Evans,^{1,4} Stuart M. Aston,⁵ TJ Shaffer,³ Arnaud Pele,⁵ Janeen H. Romie,⁵ Betsy Weaver,³ Peter Fritschel,¹ Nergis Mavalvala,^{1,4} and Fabrice Matichard^{1,6}

¹⁾ *LIGO, Massachusetts Institute of Technology, Cambridge, MA 02139, USA*

²⁾ *Mechanical Engineering Department, MIT, Cambridge, MA 02139, USA*

³⁾ *LIGO Hanford Observatory, Richland, WA 99352, USA*

⁴⁾ *Physics Department, MIT, Cambridge, MA 02139, USA*

⁵⁾ *LIGO Livingston Observatory, Livingston, LA 70754, USA*

⁶⁾ *LIGO, California Institute of Technology, Pasadena, CA 91125, USA*

(Dated: 15 December 2024)

We present a tabletop six-axis vibration isolation system, compatible with Ultra-High Vacuum (UHV), which is actively damped and provides 25 dB of isolation at 10 Hz and 65 dB at 100 Hz. While this isolation platform has been primarily designed to support optics in the LIGO detectors, it is suitable for a variety of applications. The system has been engineered to facilitate the construction and assembly process, while minimizing cost. The platform provides passive isolation for six degrees of freedom of passive isolation using a combination of vertical springs and horizontal pendula. It is instrumented with voice-coil actuators and optical shadow sensors to damp the resonances. All materials are compatible with stringent vacuum requirements. Thanks to its architecture, the system's footprint can be adapted to meet spatial requirements, while maximizing the optical table's dimensions. Three units are currently operation for LIGO. We present the system's design, controls principles, and experimental results.

I. INTRODUCTION

Many precision measurement experiments must be performed in a seismically isolated environment¹ and under vacuum^{2,3} to achieve their designed sensitivity. We present an Ultra-High Vacuum (UHV) compatible tabletop 6-axis vibration isolation system, with integrated active damping control, that provides three orders of magnitude of isolation above 100 Hz. This system has been designed to provide isolation to a new component of the Advanced LIGO interferometers⁴, a squeezed light source (the Vacuum Optical Parametric Oscillator, VOPO) that aims to improve the interferometers' sensitivity by reducing quantum shot noise^{5,6}. Isolation is obtained by a combination of vertical springs and horizontal pendula, commonly used in Advanced LIGO⁷, while voice-coil actuators provide active damping. Unlike other Advanced LIGO vibration isolation suspensions^{8,9}, the support structure is not based on a welded frame and takes advantage of independent blade posts, making its design simpler and more flexible. In particular, the dimensions of the optical table can be adapted to fit space constraints.

This paper is organized as follows: the mechanical design and both the horizontal and vertical isolation of the system are described in Sec. II; active damping control topology is presented in Sec. III; and in Sec. IV we discuss the results of experimental tests performed on the first platform prototype unit assembled at the MIT-LIGO laboratory and on the two units subsequently installed at the LIGO observatories.

II. MECHANICAL DESIGN

The system provides seismic isolation and active damping control in all six degrees of freedom. The suspended stage (stage 1) is mechanically isolated from the support base (stage 0) (see Fig. 2).

Stage 1 is suspended with three independent blade assemblies (see Fig. 3) bolted to stage 0. This approach, based on low-height posts, reduces the cost, weight, and dimensions compared to the welded support frames used in previous LIGO suspensions⁹. It maximizes the optical table dimensions with respect of the space available and makes the system adaptable to different optical table

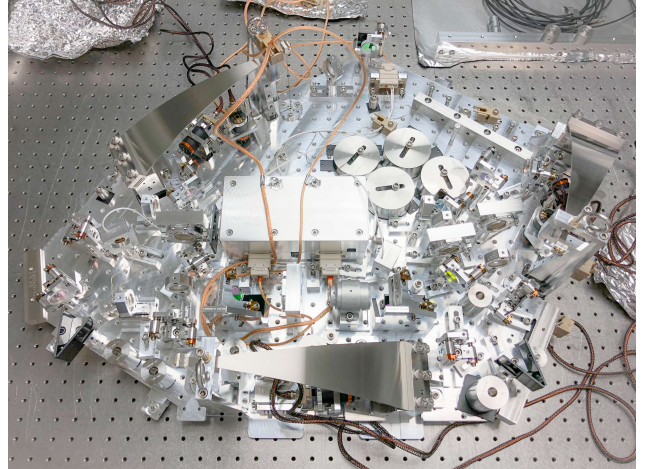


FIG. 1. **UHV COMPATIBILITY.** The isolation platform at the LIGO Livingston Observatory. All the materials fulfill stringent UHV requirements¹⁰.

^{a)} Electronic mail: alvarofg@mit.edu

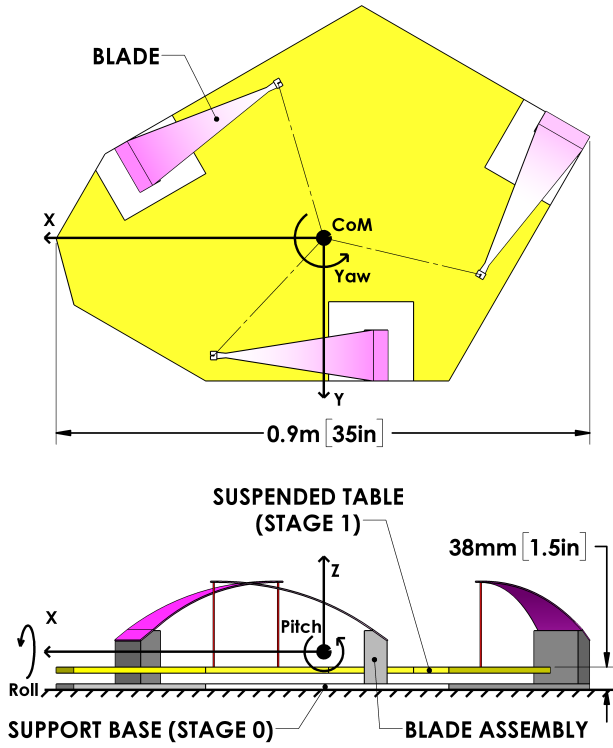


FIG. 2. **COMPACTNESS.** Schematics of the isolation platform. The optical table is suspended from three blade assemblies, 38 mm (1.5 in) above the reference plane. The footprint matches the space available in the LIGO chambers.

shapes (see Fig. 3). The number, position, and characteristics of the blade assemblies can easily be adapted to various table shapes, payloads, and performance requirements.

There are two types of resonances that are critical to the design of this type of seismic isolator: the suspension modes and the structural modes. The first are the

TABLE I. Basic platform mechanical parameters

Parameter	Value
Total dimensions	0.94 x 0.67 m [26.5 x 37 in.]
Total height	0.21 m [8.1 in.]
Total mass	45 kg
Suspended stage	
Table surface	0.34 m ² [520 in. ²]
Table height	0.38×10^{-3} m [1.5 in.]
Mass	36 kg
z_{CoM}	7.82×10^{-3} m
Inertia _{roll}	0.705 kg m ²
Inertia _{pitch}	1.313 kg m ²
Inertia _{yaw}	1.958 kg m ²

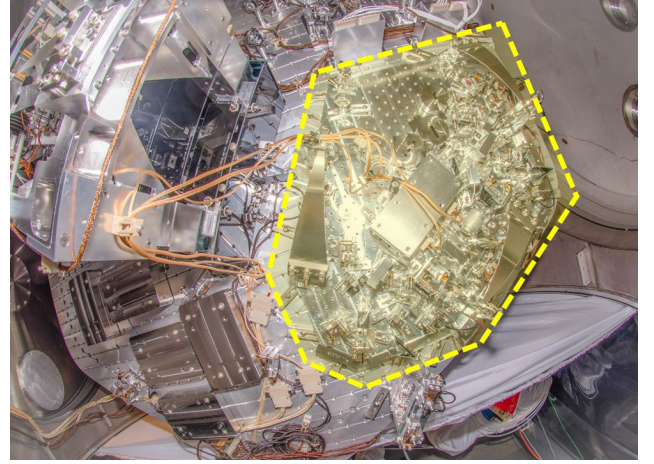
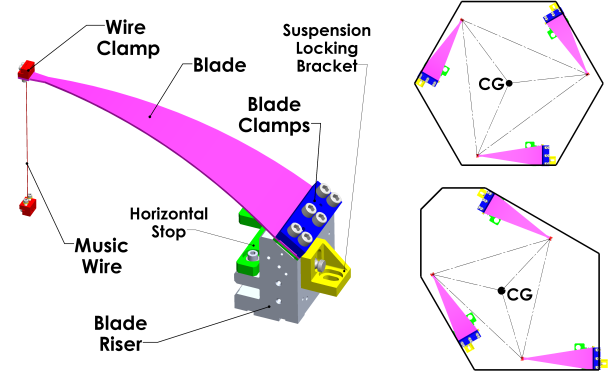


FIG. 3. **SHAPE ADAPTABILITY.** Blade assembly (top left), including the riser clamped to the base, the blade clamped at a specific angle, and the pendulum wire clamped to the tip of the blade. The blade assembly includes built-in hard stops that limit the range of motion of the optical table. Using independent blade assemblies to suspend the optical table makes the design adaptable to different requirements. As an illustration, two optical table shapes that could be isolated using this concept (top right). Our design was adapted to match the available space in the aLIGO chambers (bottom)

rigid-body modes associated with each of the six degrees of freedom. The structural modes are the flexible modes of the sub-assemblies, such as the blade assemblies or blade guards (see Fig. 4). Since suspension modes have lower frequencies than structural modes, the isolation bandwidth can be defined as the range between the highest suspension mode frequency and the lowest structural mode frequency.

LIGO's requirements⁶ drive the choice of the highest suspension mode frequency (≈ 2.5 Hz) and the lowest structural mode frequency (≈ 220 Hz). At 100 Hz, the suspension provides 65 dB of seismic isolation, and the suspension modes are actively damped to quality factors of about 15. The main parameters of the platform are specified in Table I.

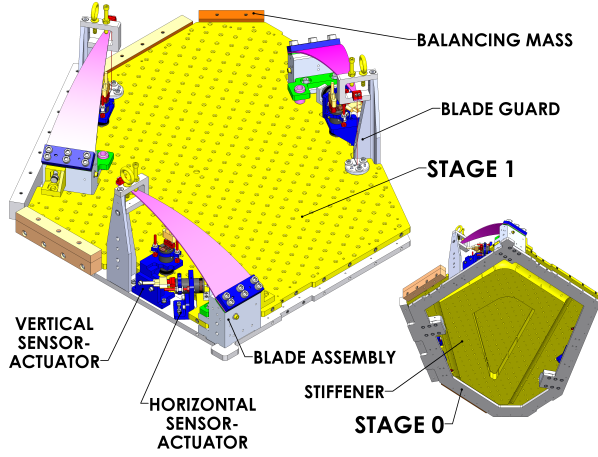


FIG. 4. **EFFECTIVE FOOTPRINT.** Most of the footprint corresponds to the optical table. The isolation platform is instrumented with six sensor-actuators positioned in vertical-horizontal pairs. The blade guards provide safety during assembly. The optical table features a stiffener underneath to increase the stiffness to mass ratio.

A. Ultra-high vacuum compatibility

All the materials used in the isolation platform are approved for ultra-high vacuum applications and fulfill LIGO vacuum system specific requirements¹⁰. Before final assembly, all the components are precision cleaned and vacuum baked. In addition, a residual gas analysis is performed after baking to measure the outgassing rate and detect possible residual contamination.

B. Suspended stage

The suspended stage consists of an optical table ($\approx 0.34 \text{ m}^2$, $\approx 18 \text{ kg}$), optical components ($\approx 11 \text{ kg}$), and balancing masses ($\approx 7 \text{ kg}$) used to level the platform. The table shape is adapted to the available space in the LIGO vacuum chamber¹¹, resulting in the heptagonal shape shown in Fig. 1.

The first structural mode is a bending resonance of the suspended table. To raise its frequency, a stiffener is incorporated into the optical table (see Fig. 4). The shape of the stiffener has been designed to optimize the stiffness to mass ratio. This optimization is performed iteratively using Finite Element Analysis (FEA) of the loaded optical table. Fig. 5 shows the results of this optimization, with the first resonance at $\approx 225 \text{ Hz}$.

C. Horizontal isolation

Horizontal isolation (X-Y-Yaw axis in Fig. 2) is achieved by suspending stage 1 from three wires. The pendulum is a simple and effective way to provide passive horizontal isolation. The wires are attached using metal clamps designed to reduce friction losses. The horizontal modes frequencies can be approximated using Eq.

(1).

$$f_{xx} = f_{yy} = \frac{1}{2\pi} \sqrt{\frac{k_{xx}}{m}} \quad (1)$$

where k_{xx} and m are, respectively, the horizontal stiffness and supported mass of each wire. The stiffness can be estimated using Eq. (2).

$$k_{xx} = k_{yy} = \frac{mg}{l_w - 2z_{\text{ZMP}}} \quad (2)$$

where l_w is the length of the wires and z_{ZMP} is the vertical distance from the wire tip to the Zero Moment Point (ZMP), which can be estimated as:

$$z_{\text{ZMP}} = \sqrt{\frac{E_w I_w}{mg}} \tanh \frac{mgl_w}{2E_w I_w} \quad (3)$$

E_w being the wire Young's modulus.

The suspension wires are made of stainless steel; they are 146 mm long and 0.61 mm in diameter. The horizontal suspension frequency (1.27 Hz) and the factor of safety (>3) can be approximated using the following equations:

$$\sigma_{\text{VM}}^w = \sqrt{\sigma_{\text{max}}^2 + \tau_{\text{max}}^2} \quad (4)$$

$$\text{FoS}_w = \frac{\sigma_{\text{VM}}^w}{\sigma_{\text{yield}}^w} \quad (5)$$

where τ_{max} and σ_{max} are, respectively, the maximum shear and normal stress at the wire for a given horizontal displacement. σ_{VM} is the equivalent Von Mises stress, and σ_{yield} is the yield strength of the wire. The maximum

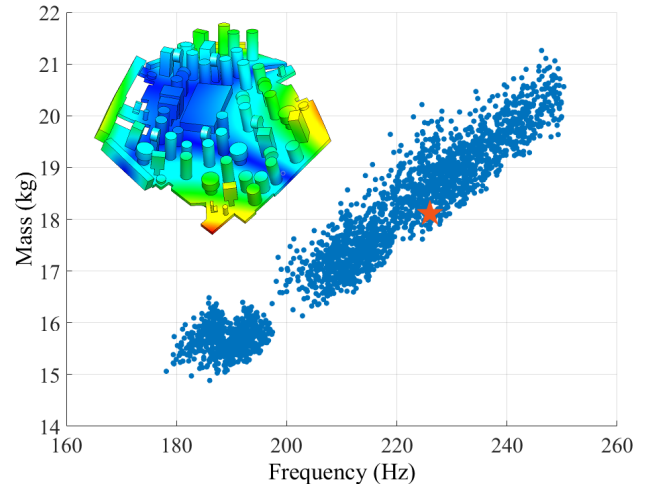


FIG. 5. **TABLE STIFFNESS.** Results of the table stiffener optimization. Using iterative finite element analysis on the optical table for different stiffener shapes and sizes. The selected dimension (indicated with a star) was chosen to have the highest stiffness to mass ratio while meeting the requirements on total mass and center of mass position.

stresses are estimated with Eq. (7) and Eq. (6).

$$\sigma_{\max}^w = \frac{mg}{A_w} + \frac{mgz_{\text{ZMP}}d\delta}{2I_w(l_w - 2z_{\text{ZMP}})} \quad (6)$$

$$\tau_{\max}^w = \frac{mg\delta}{A_w(l_w - 2z_{\text{ZMP}})} \quad (7)$$

where δ is the maximum lateral displacement of the wire ends (1 mm for this platform), d_w is the diameter of the wire, and $A_w = \frac{\pi d_w^2}{4}$ is its cross section area. These formulas account for the normal axial stress, shear stress, and bending stress, the latter being predominant in this design.

The wire diameter is small enough to place the violin modes at frequencies much higher than the blade vertical mode (~ 763 Hz). The approximate formula for the modes (which takes into account some anharmonicity due to the elasticity of the wires) is¹²:

$$f_{\text{VIOLIN}} = \sqrt{\frac{T}{\rho_w A_w} \frac{n\pi}{l_w} \left(1 + \frac{2\Delta}{l} + \left(\frac{2\Delta}{l} \right)^2 + \left(\frac{n\pi\Delta}{l} \right)^2 \right)} \quad (8)$$

where $T = mg$ is the tension on the wire, ρ is the density of the wire, n is the mode number, and $\Delta = \sqrt{E_w I_w / T}$ is a parameter representing the distance over which the wire bends near the clamps (~ 3.4 mm for our platform).

D. Vertical isolation

The vertical isolation is provided by three triangular stainless steel cantilever blade springs. This shape guarantees an homogeneous stress distribution (assuming infinitesimal strain). The vertical stiffness (k_{zz}) and first resonance (f_{zz}) of the blades can be approximated by Eq. (9) and Eq. (10), respectively.

$$k_{zz} = \sqrt{\frac{E_b a_b h_b^3}{6l_b^3}} \quad (9)$$

TABLE II. Basic isolation platform mechanical parameters

Parameter	Value
Design parameters	
Wire length (l_w)	145.6×10^{-3} m
Wire diameter (d_w)	0.61×10^{-3} m
Modeled results	
Horizontal resonance f_{xx}	1.26 Hz
Spring constant (single blade) k_{xx}	$790.5 \frac{\text{N}}{\text{m}}$
z_{ZMP}	3.41×10^{-3} m
FoS _w	3.65

$$f_{zz} = \frac{1}{2\pi} \sqrt{\frac{k_{zz}}{m}} \quad (10)$$

where E_b is the blade Young's modulus, a_b is the width of the blade at the base, h_b is the blade thickness, m is the mass supported by each blade, and l_b is the length of the blade.

Using infinitesimal strain theory, we can estimate the vertical deflection (ω_{tip}) and angle (ω'_{tip}) at the tip of the blade (Eq. 11), as well as their maximum stress and factor of safety (Eq. 12).

$$\omega_{\text{tip}} = \frac{6mgl_b^3}{E_b a_b h_b^3} \quad \omega'_{\text{tip}} = \frac{12mgl_b^2}{E_b a_b h_b^3} \quad (11)$$

$$\sigma_{\max}^b = \frac{6mgl_b}{a_b h_b^2} \quad \text{FoS}_b = \frac{\sigma_{\max}^b}{\sigma_{\text{yield}}^b} \quad (12)$$

Since there are three design parameters (a_b , l_b , and h_b) and only two constraints (f_{zz} and σ_{\max}^b from Eq. (10) and Eq. (12)), the design has one degree of freedom. For our suspension we defined the length l_b to be well suited to the overall dimensions of the platform.

The blades are made from grade 440C stainless steel and are manufactured flat. This reduces the cost and lead-time compared to previous aLIGO blades¹³. However, maraging steel is recommended if creep noise or crackle are a concern¹⁴. Design values are given in Table III.

The preliminary design is performed using Eq. (10-12), which assume classical infinitesimal strain beam theory. The blade stiffness and peak stress estimates are verified with finite element analysis. The relative error between the two calculations is around 1 % in deflection and 7 % in stress, as shown in Fig. 6.

The height and angle of the base of the blade assembly are determined using FEA to accurately predict the deformation of the blade. Contact analysis was used to de-

TABLE III. Basic isolation platform mechanical parameters

Parameter	Value
Design parameters	
Blade base width a_b	85×10^{-3} m
Blade thickness h_b	2.11×10^{-3} m
Blade length l_b	280×10^{-3} m
Young's modulus E_b	2.1×10^{11} Pa
Modeled results	
Vertical resonance f_{zz}	1.64 Hz
Spring constant k_{zz}	$1273.1 \frac{\text{N}}{\text{m}}$
Tip deflection ω_{tip}	92.5×10^{-3} m
Tip rotation ω'_{tip}	0.66 rad
FoS _b	3.44

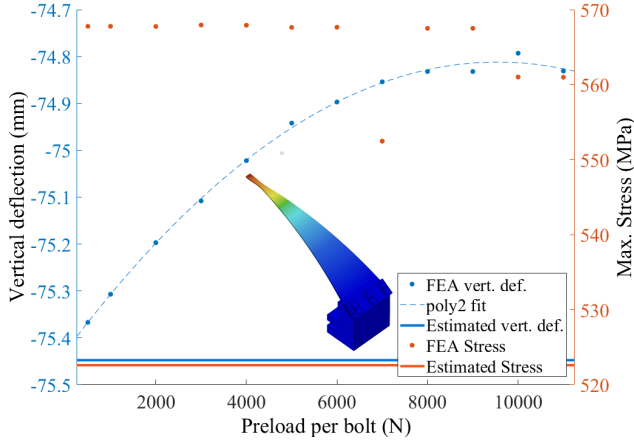


FIG. 6. **CLAMP DESIGN.** Results from the FEA for the blade post. The FEA includes the preload in the blade clamp as a parameter and, for each level of preload, the vertical deflection of the blade's tip and the maximum stress in the blade are calculated (points) and compared with their theoretical estimated values (solid lines). This analysis shows the appearance of compliance (more vertical deflection) due to lack of preload. For this specific situation (post pitch angle of 35.32°), the minimum amount of preload is ≈ 8000 N. This type of analysis is used to define the right blade post angle and preload at the clamp to ensure that the nominal position of the optical table is reached for the desired mass.

fine adequate clamping and bolt preload condition (Fig. 6).

Due to its annular shape, stage 0 has low torsional stiffness and relies on being well clamped to the support structure. FEA was used to evaluate the number of clamping elements necessary to establish good contact, and results were verified by experiment.

The rotational stiffness of the isolation system can be estimated using the translation stiffness and the geometrical location of the blade tips as shown in Eq. (13) and Eq. (14) for an equilateral triangular distribution.

$$k_{\text{roll}} (= k_{\text{pitch}}) = \frac{3}{2} k_{zz} R^2 + 3 k_{yy} h_z^2 - 3 m g h_z \quad (13)$$

$$k_{\text{yaw}} = \frac{3}{2} (k_{xx} + k_{yy}) R^2 + 3 \frac{G_w I_w}{l_w} \quad (14)$$

where $h_z = z_{\text{CoM}} - z_{\text{ZMP}}$ is the vertical offset between the center of mass (CoM) and the ZMP, G_w is the shear modulus of the wire, and R is the horizontal distance between the center of gravity and the tip of the blades.

Due to the vertical offset between the CoM and the ZMP (h_z), some of the modes are coupled. This leads to off-diagonal terms in the 6x6 stiffness matrix (Eq. 15).

$$\mathbf{K} = \begin{bmatrix} 3k_{xx} & 0 & \kappa_{xz} & 0 & 3k_{xx}h_z & 0 \\ 0 & 3k_{yy} & \kappa_{yz} & 3k_{yy}h_z & 0 & 0 \\ \kappa_{xz} & \kappa_{yz} & 3k_{zz} & 0 & 0 & \kappa_{zrz} \\ 0 & 3k_{yy}h_z & 0 & 3k_{\text{roll}} & \kappa_{rxy} & 0 \\ 3k_{xx}h_z & 0 & 0 & \kappa_{rxy} & 3k_{\text{pitch}} & 0 \\ 0 & 0 & \kappa_{zrz} & 0 & 0 & 3k_{\text{yaw}} \end{bmatrix} \quad (15)$$

Furthermore, the blades are not flat when the suspension is floated (Fig. 3) and their axes do not form an equilateral triangle (Fig. 4). These effects also introduce cross-coupling between the modes (κ_{ij}). Their values can be approximated with an analytic expression, but the derivation is out of the scope of this paper. However, one of the design considerations taken into account is to reduce the vertical offset between the CoM, the ZMP, and the horizontal actuation plane (i.e., the height of the horizontal actuators). Note that the zeros in the stiffness matrix (Eq. 15) represent couplings that are not relevant in our design but that could potentially be relevant for a different blade distribution.

Due to the cross couplings, the resonant frequencies are better approximated solving the eigenvalue problem in Eq. 16.

$$[\mathbf{M}^{-1}\mathbf{K}] \phi_n = -(2\pi f_n)^2 \phi_n \quad (16)$$

where \mathbf{M} is the mass matrix, f_n is the n^{th} resonant frequency, and ϕ_n is the mode shape of that resonance. The results of this calculation are summarized in Tab. IV.

III. ACTIVE DAMPING CONTROL

Since the system has low loss (i.e., high Q), the suspension modes must be damped to avoid excessive motion at the resonances.

The LIGO Scientific Collaboration (LSC) has produced two types of low-noise ultra-high vacuum compatible collocated actuator-sensor pairs, named AOSEM and BOSEM^{15,16}. Their actuation strengths are 0.0309 N/A and 1.694 N/A, respectively. The main options to damp the isolation platform are:

- Eddy Current Damper: passive, no-noise, simple
- AOSEM: active, low noise, compact, low-cost
- BOSEM: active, low noise, high strength

We use active voice-coil dampers instead of passive dampers (eddy-current) because they provide better control of the damping performance without compromising the passive isolation. Eddy current dampers can reduce the isolation at 100 Hz relative to other options. For a similar level of damping (Qs smaller than 100), eddy current dampers will reduce the isolation by 15 dB the isolation at 100 Hz (see Fig. 7). Note that in this calculation the sensor and actuator noises were not taken into account. Their effect is discussed in Sec. III.B.

Furthermore, we chose AOSEMs over BOSEMs because we do not require the ability to steer the platform.

A. AOSEM sensor-actuator

Fig. 8 shows AOSEMs' basic principle, where a nickel plated SmCo magnet acts both as a flag sensor and as the actuation element with the coil. An electrical current in each voice-coil generates a magnetic field, which acts on the magnets attached to stage 1. The isolation platform is equipped with six AOSEMs, distributed in horizontal-vertical pairs as shown in Fig. 4, damping the degrees of freedom.

The operation point is such that the flag covers 50% of the range of the sensor when stage 1 is floating at its equilibrium position. In order to prevent sensor damage, the suspension has hard stops that limit its translation to less than 1mm (see Fig. 3).

B. Control scheme and noise budget

Fig. 9 shows the control scheme and the sources of noise, mainly the sensor, analog-to-digital (ADC), and digital-to-analog (DAC) converter noises. A simplified version of the seismic path plant (P_s) and the force path plant (P_f) in the s -domain are presented in Eq. (17) and Eq. (18), which do not take into account any cross-couplings between the degrees of freedom.

$$P_s = \frac{cs + k}{ms^2 + cs + k} \quad (17)$$

$$P_f = \frac{1}{ms^2 + cs + k} \quad (18)$$

where s is the Laplace complex variable. These equations are analogous to a single damped spring-mass system of mass m , stiffness k , and Q-factor $Q = \frac{1}{2\zeta} = \frac{\sqrt{km}}{c}$.

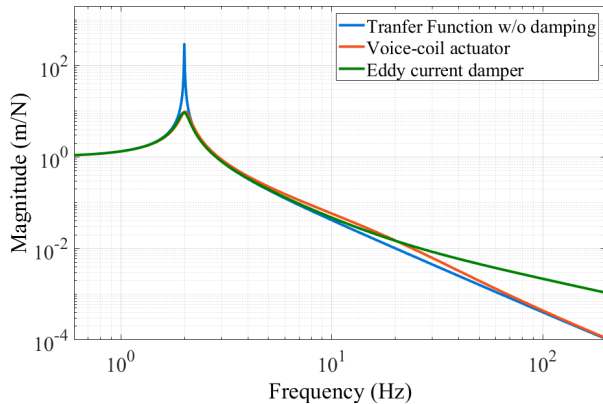


FIG. 7. **DAMPING.** Numerical comparison of the performance of the damping possibilities. This figure shows the performance of voice-coil actuation and eddy current dampers when damping a resonance at 2Hz with an initial Q of 300 (typical value for the suspensions) to a Q of 10. The voice-coil actuator uses a controller with 1 zero at DC and 2 poles, while the eddy current damper is simulated as a pure velocity controller. The passive damper reduces isolation at high frequencies (≈ 15 dB at 100Hz).

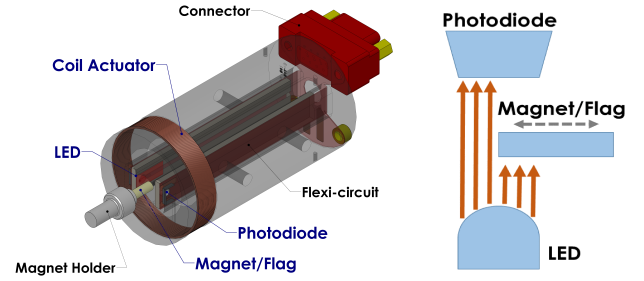


FIG. 8. **LOW NOISE, UHV COMPATIBLE ACTUATOR.** AOSEM schematics. Motion is sensed with a LED-Photodiode shadow sensor. At the nominal position, the flag (magnet) covers the shadow sensor at 50% of its full range. The actuation is provided by the coil-magnet pair. An electrical current through the AOSEM's coil generates a magnetic field, which acts on the magnet.

Given this control scheme, the ground motion (X_0), the sensor noise (N_s)¹⁷, and ADC/DAC noises (N_{DAC} , N_{ADC})^{18,19}, we can estimate the platform motion (X_1) as it follows:

$$X_1 = P_f F + P_s X_0 \quad (19)$$

where F is the force applied by the actuators, which can be calculated using the gains defined in Figure 9 as:

$$F = [G_{MAG} G_{DRV}] N_{DAC} + [G_{MAG} G_{DRV} G_{DAC} C G_{ADC}] \times N_{DAC} + [G_{MAG} G_{DRV} G_{DAC} C G_{ADC} G_{AMP} G_S] \times (N_s + X_0 - X_1) \quad (20)$$

Given that the noise sources are incoherent, we can estimate the total noise using their root mean square (RMS):

$$|X_1|^2 \sim |X_{X_0}|^2 + |X_{N_{ELEC}}|^2 \quad (21)$$

where the platform's motion due to ground seismic mo-

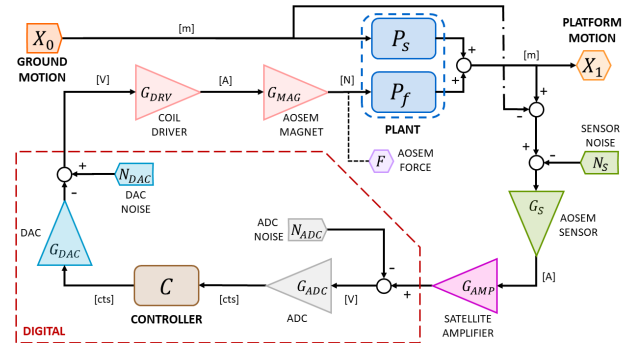


FIG. 9. **CONTROL SCHEME.** Control scheme of the isolation platform at the aLIGO observatories. The analog signal from the AOSEMs is digitized before it is sent to the controller, which generates a signal that is converted and sent to the AOSEMs' coil driver. Besides seismic noise, this scheme introduces electronic noise due to the sensor, the analog-to-digital (ADC), and digital-to-analog (DAC) converters.

tion can be estimated as:

$$X_{X_0} = \frac{RR + P_s}{1 + RR} X_0 \quad (22)$$

where RR is the return ratio (i.e., the open loop):

$$RR = P_f G_c \quad (23)$$

Defining $G_F = G_{MAG} G_{DRV}$, $G_{AS} = G_{AMP} G_S$, and $G_{AD} = G_{DAC} G_{ADC}$, we have that:

$$G_c = G_F G_{AS} G_{AD} C \quad (24)$$

For a given controller, the total electronic noise corresponds to:

$$|X_{N_{ELEC}}|^2 \sim |X_{N_{DAC}}|^2 + |X_{N_{ADC}}|^2 + |X_{N_S}|^2 \quad (25)$$

where

$$X_{N_{DAC}} = \frac{P_f G_F}{1 + RR} N_{DAC} \quad (26)$$

$$X_{N_{ADC}} = \frac{1}{G_{AS}} \frac{P_f G_C}{1 + RR} N_{ACD} \quad (27)$$

$$X_{N_S} = \frac{P_f G_C}{1 + RR} N_S \quad (28)$$

The contribution of these terms to the closed loop motion is quantified and discussed in section IV.C.

IV. EXPERIMENTAL PERFORMANCE

A prototype of the platform was tested at the MIT-LIGO facilities and two units have been installed at the LIGO observatories in Livingston, LA (LLO) and Hanford, WA (LHO). The results presented in this section

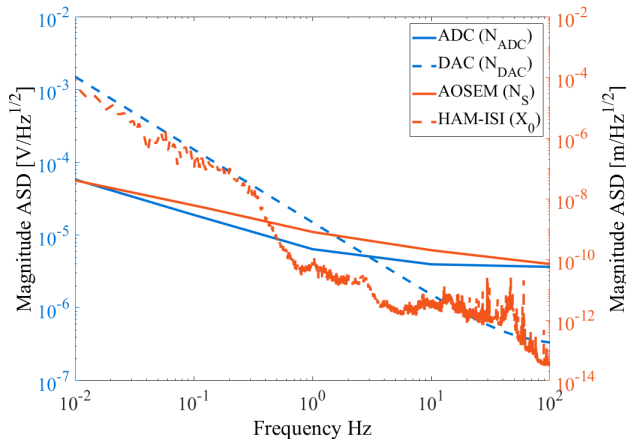


FIG. 10. **INPUT NOISE.** The platform is to be mounted on an isolated HAM-ISI table¹¹. The input motion of our system (X_0) is the motion of the HAM-ISI. This figure also presents the noise characteristics of both the sensor and the digitization electronics.

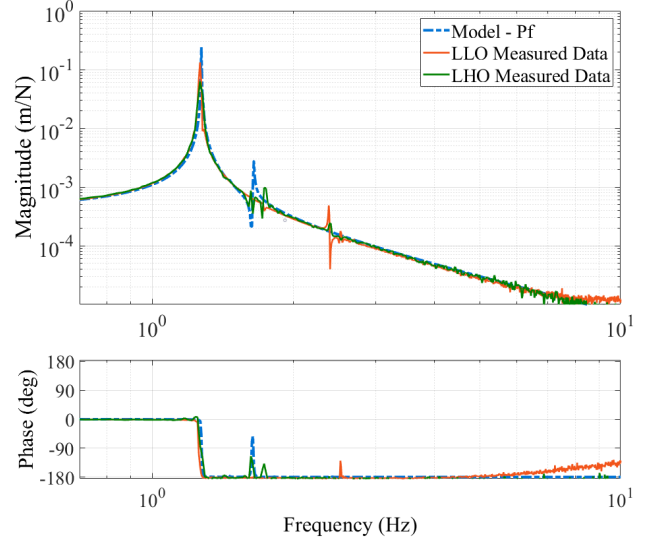


FIG. 11. **TRANSFER FUNCTIONS** Longitudinal (X) transfer function measured at LLO and LHO, DC calibrated to match the dynamical model. The data shows f^2 isolation above the resonance.

are from testing these three units.

A. Transfer functions

The transfer functions were obtained by driving the coils and reading out the shadow sensors of the AOSEMs. Fig. 11 shows an example of the suspension's transfer function. Rigid body mode frequencies and Q-factors are summarized in Table IV.

B. Structural modes

The light and low-profile supporting structure reduces the system's impact on neighboring elements. Experimental modal analysis of the optical table is consistent with the FEA predictions, as shown in Fig. 12. This response was obtained using a B&K 8206 Impact Hammer and a miniature triaxial accelerometer type 4506 B on the fully loaded suspension. The measured resonances are consistent with predictions for the structural resonances

TABLE IV. Rigid body modes

Degree-of-freedom	Measured (Model) Q-factor	
Longitudinal-X	1.27 (1.26) Hz	260
Transverse-Y	1.27 (1.28) Hz	310
Vertical-Z	1.74 (1.64) Hz	250
Roll-RX	2.39 (2.23) Hz	170
Pitch-RY	1.63 (1.56) Hz	200
Yaw-RZ	1.44 (1.44) Hz	250

of the elements of the suspension. In order to damp the main structural mode, we introduced constrained layer dampers (i.e., Viton pads between the balancing masses and the optical table). Fig. 12 also shows the effect of those dampers, reducing the Qs by about a factor of 2-3.

C. Active Damping

Our damping control uses the platform's global Cartesian basis via matrix transformations from local to global bases²⁰.

The controller (C) is a band-pass filter of the form:

$$C(s) = K \frac{s}{\left(\frac{s}{2\pi f_1} + 1\right) \left(\frac{s}{2\pi f_2} + 1\right)} \quad (29)$$

with one zero at DC and two poles at frequencies f_1 and f_2 . The idea is to have velocity damping at the resonance and to prevent the injection of noise at high frequencies. This controller is sufficient to bring the Q values to less than 20 with minimal degradation of the passive isolation, as shown in Fig. 13. This figure also shows that the real implementation does have a perfect velocity damper at the resonance (filter phase $\approx 60^\circ$), introducing some stiffness to the system, which explains the resonance shift to a slightly higher frequency.

Fig. 14 shows the motion of the platform with and without active damping. The control loops reduce the RMS motion by an order of magnitude with no measurable motion amplification. The motion amplification at high frequency is quantified by noise budgeting.

An example noise budget is shown in Fig. 15. It shows that the platform motion due to the control electronics comes predominantly from sensor noise at low frequencies and ADC noise at high frequencies. Fig. 15 also compares the estimated platform motion due to the electronics and to the seismic motion on top of the pre-isolator (HAM-ISI). For the given controller, these are within an order of magnitude at the resonance. Fig. 15 also com-

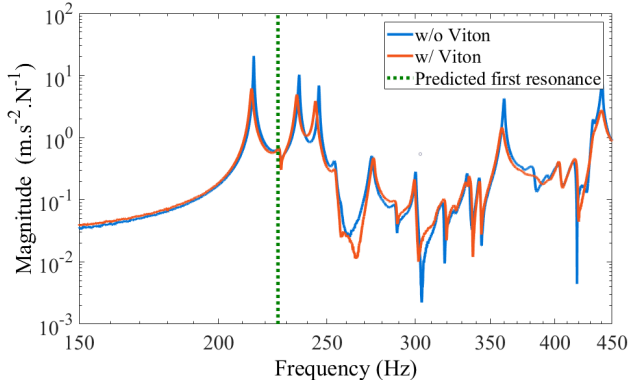


FIG. 12. **BANDWIDTH.** Modal analysis results for the vertical (Z) degree of freedom. The Viton pads reduce the mode Qs by about a factor of 2-3. The first resonance is slightly lower than predicted (because the final optics configuration was different than the model) but it is still higher than the required 200 Hz.

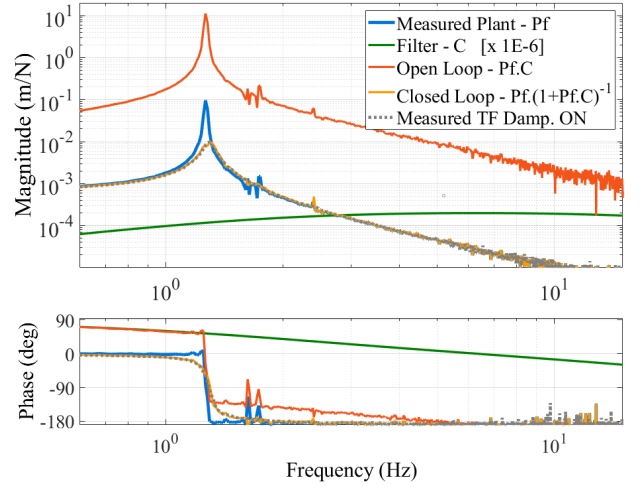


FIG. 13. **ACTIVE DAMPING.** Damping control for the longitudinal (X) degree of freedom. Using a band-pass filter (brown), the Q is reduced from ≈ 260 (blue) to ≈ 15 (orange) without degrading the isolation. The phase margin of the controller is $\approx 53^\circ$ (red). The damped transfer function was measured (grey) and matches the model.

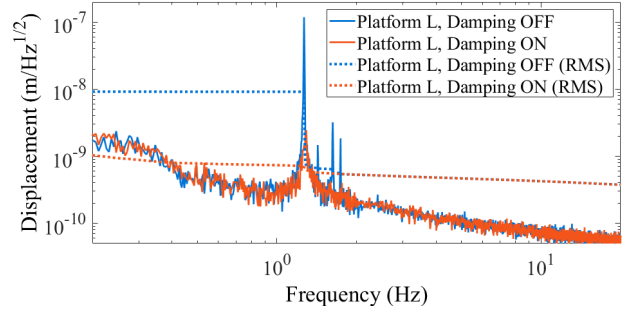


FIG. 14. **MOTION REDUCTION.** Relative displacement ($X_1 - X_0$) power spectrum when the damping loops are ON (red) and OFF (blue) for the longitudinal (X) degree of freedom. The damping results in a reduction of one order of magnitude in RMS relative motion.

pares the motion of the platform (green) with the input motion at its base (X_0 , blue), showing explicitly the effect of the presented isolator. Since the pre-isolator makes the input motion (X_0) particularly low, the electronic noise dominates the output motion at frequencies above 3 Hz. Depending on input motion and applications, this controller can be tuned for a different compromise over the frequency range. In particular, we observe that, for a band-pass controller, the compromise is between the level of damping at resonance and electronic noise injection at high frequency.

V. CONCLUSION

We present a compact isolation platform designed to support LIGO auxiliary optics emphasizing the system's compactness, simplicity, and UHV characteristics. This paper describes the active damping implemented to

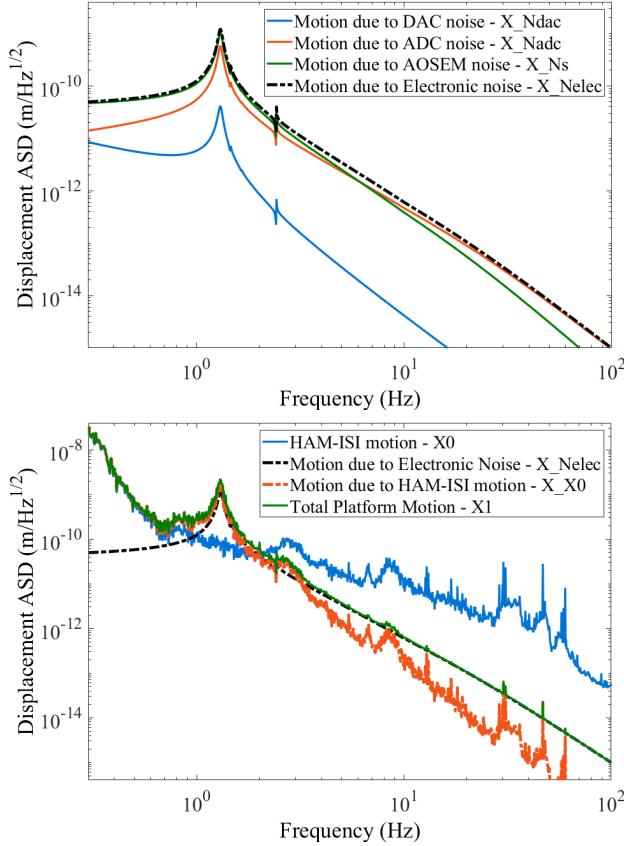


FIG. 15. **NOISE BUDGET.** Noise budget for the transverse (Y) degree of freedom. (Top) Estimate of the platform motion due to each noise source. At low frequencies, the sensor noise predominates, whereas high frequencies are dominated by ADC noise. (Bottom) The total motion produced by the damping control electronics (dashed black) is compared to the estimated motion produced by the HAM-ISI seismic motion (dashed orange). In this example, the electronics are the main source of platform motion above 3 Hz. This figure also shows a comparison between the HAM-ISI motion (X_0) and the total motion of the suspended stage (X_1).

preserve passive isolation. Experimental measurements show good agreement between predicted and measured performance. Thanks to its adaptable design and low production cost, this isolation system was easily procured and deployed at the LIGO sites and can be easily adapted to other applications.

ACKNOWLEDGMENTS

We wish to thank Norna Robertson and Calum Torrie from LIGO-Caltech for their help in designing the VOPO suspension, as well as the people from the aLIGO

Livinston and Hanford observatories for their help during testing and installation.

LIGO was constructed by the California Institute of Technology and Massachusetts Institute of Technology with funding from the National Science Foundation, and operates under cooperative agreement PHY0757058. Advanced LIGO was built under award PHY0823459. This paper was assigned LIGO Document Number LIGO-P1800182.

- ¹X. Wu, F. Zi, J. Dudley, R. J. Bilotta, P. Canoza, and H. Müller, arXiv preprint arXiv:1707.08693 (2017).
- ²W. Meng, Y. Guo, Y. Hou, and Q. Lu, *Nano Research* **8**, 3898 (2015).
- ³M. Jaffe, P. Haslinger, V. Xu, P. Hamilton, A. Upadhye, B. Elder, J. Khoury, and H. Müller, *Nature Physics* **13**, 938 (2017).
- ⁴B. Abbott, R. Abbott, R. Adhikari, P. Ajith, B. Allen, G. Allen, R. Amin, S. Anderson, W. Anderson, M. Arain, *et al.*, *Reports on Progress in Physics* **72**, 076901 (2009).
- ⁵L. S. Collaboration *et al.*, *Nature Physics* **7**, 962 (2011).
- ⁶J. Aasi, B. Abbott, R. Abbott, T. Abbott, M. Abernathy, K. Ackley, C. Adams, T. Adams, P. Addesso, R. Adhikari, *et al.*, *Classical and quantum gravity* **32**, 074001 (2015).
- ⁷F. Matichard, B. Lantz, R. Mittleman, K. Mason, J. Kissel, B. Abbott, S. Biscans, J. McIver, R. Abbott, S. Abbott, *et al.*, *Classical and Quantum Gravity* **32**, 185003 (2015).
- ⁸N. Robertson, D. Bridges, M. Barton, J. Heefner, M. Meyer, J. Romie, C. Torrie, J. Lewis, S. Barnum, and J. Kissel, “OMC suspension final design document,” Tech. Rep. LIGO-T0900060 (LIGO Laboratory, 2009).
- ⁹N. Robertson, D. Bridges, M. Barton, J. Heefner, J. Romie, C. Torrie, and J. Kissel, “Ham large triple suspension (hlts) final design document,” Tech. Rep. LIGO-T1000012-v6 (LIGO Laboratory, 2013).
- ¹⁰D. Coyne *et al.*, “LIGO vacuum compatible materials list,” Tech. Rep. LIGO-E960050-v12 (LIGO Laboratory, 2013).
- ¹¹F. Matichard, B. Lantz, K. Mason, R. Mittleman, B. Abbott, S. Abbott, E. Allwine, S. Barnum, J. Birch, S. Biscans, *et al.*, *Precision Engineering* **40**, 273 (2015).
- ¹²G. I. González and P. R. Saulson, *The Journal of the Acoustical Society of America* **96**, 207 (1994).
- ¹³M. Plissi, “Cantilever blade analysis for Advanced LIGO,” Tech. Rep. T030107-00-D (LIGO Science Collaboration, 2003).
- ¹⁴B. Levi, “Working towards finding an upper limit for crackle in ligo’s maraging steel blade springs,” Tech. Rep. LIGO-T1300839 (LIGO Laboratory, 2014).
- ¹⁵S. M. Aston, *Optical read-out techniques for the control of test-masses in gravitational wave observatories*, Ph.D. thesis, University of Birmingham (2011).
- ¹⁶L. Carbone, S. Aston, R. Cutler, A. Freise, J. Greenhalgh, J. Heefner, D. Hoyland, N. Lockerbie, D. Lodhia, N. Robertson, *et al.*, *Classical and Quantum Gravity* **29**, 115005 (2012).
- ¹⁷S. Aston, “Advanced ligo bosem noise measurement report,” Tech. Rep. LIGO-T0900496-v4 (LIGO Laboratory, 2011).
- ¹⁸J. Heefner, “Preliminary noise measurements of the general standards pci66-16ai64ssa-64-50m adcs,” Tech. Rep. LIGO-T060158-x0 (LIGO Laboratory, 2006).
- ¹⁹R. Mittleman, “16 bit low frequency dac noise measurement,” Tech. Rep. LIGO-T1500007-v1 (LIGO Laboratory, 2015).
- ²⁰F. Matichard, J. Kissel, and C. Ramet, “aLIGO SEI actuators and sensors change of basis (transformation, orientation),” Tech. Rep. LIGO-T1000388-v17 (LIGO Laboratory, 2014).